Parametric amplification of optical phonons

Supporting Information

A. Cartella[1], T. F. Nova[1,2], M. Fechner[1], R. Merlin[3] and A. Cavalleri[1,2,4]

[1]Max Planck Institute for the Structure and Dynamics of Matter, Hamburg, Germany

[2]The Hamburg Centre for Ultrafast Imaging, Hamburg, Germany

[3]Department of Physics, University of Michigan

[4]Department of Physics, Clarendon Laboratory, University of Oxford, Oxford, UK

www.pnas.org/cgi/doi/10.1073/pnas.1809725115

S1 – Experimental set-up

Laser pulses with 5.5 mJ energy, 800 nm wavelength and 100 fs duration at 1 KHz repetition rate from a commercial Ti:Sapphire regenerative amplifier were split into three parts (80%, 15%, 5%).

The 80% beam was used to pump a pair of two-stage optical parametric amplifiers (OPAs), seeded by the same white light continuum (WLC) and delivering phase-locked signal output pulses in the near infrared (300 μJ, 70 fs duration, tuned at 1.46 and 1.28 μm wavelength, respectively). The difference frequency generation (DFG) in a GaSe crystal between these signals delivered carrier envelope phase (CEP) stable [1] mid-infrared pump pulses of 130 fs duration, 29 THz center frequency, and up to 10 μJ energy. These pulses were transmitted through a pair of KRS-5 broadband wire grid polarizers (used to vary their intensity) and focused at normal incidence onto the sample with a 150mm effective focal length off-axis parabolic mirror. The beam diameter at the sample position, measured by its transmission through a calibrated pin-hole, was about 240 μm, yielding to a maximum fluence of 13 mJ/cm^2, corresponding to 8.68 MV/cm peak electric field.

The 15% beam was used to pump a similar setup, with two OPAs seeded by the same WLC and tuned at 1.45 μm and 1.29 μm, respectively. The DFG between these signals produced mid-infrared probe transients at 26.5 THz, with 100 fs duration and energy of 0.6 μJ. These were attenuated with a pair of gold wire grid polarizers and focused on the sample at 15 degrees from normal incidence. The probe spot size on the sample, also measured by its transmission via a calibrated pin-hole, was 170 μm. The reflected pulses were then collimated and steered towards the electro-optic sampling (EOS) setup [2], where their electric field profile could be measured. The optical path of the probe pulses between the sample and the EOS setup was long enough to prevent any possible scattered pump light from being detected, owing also to the very good sample surface quality. This was properly checked by running test measurements in which the probe pulses were blocked, and making sure that no signal was detected in the EOS. Figure S1-1 shows a sketch of the measurement setup.

The 5% beam was frequency doubled and used to pump a non-collinear optical parametric amplifier (NOPA) [3], delivering near-infrared pulses with a spectrum centered at 900nm, and

with a 60nm bandwidth. These pulses were then compressed down to approximately 20 fs duration by several bounces on a chirp-mirrors pair and used as a gate in the EOS setup. A schematic representation of the overall experimental setup including the generation of the pump, probe and gate pulses is shown in Fig. S1-2.

To accurately measure the optical properties of the sample, a double optical chopping scheme was used [4]. This allowed for the simultaneous measurement of the equilibrium and pump-induced reflected electric fields, and to calculate $\Delta E(t,\tau)/E(t,\tau)$, where t is the time delay between the pump and the probe pulses and τ the EOS time coordinate. From this ratio, the complex reflectance $\Delta r(t,\omega)/r(t,\omega)$ was calculated and added to the equilibrium one (retrieved from literature data [5]), thereby providing the complete optical properties of the sample as a function of both pump-probe delay and frequency. For more details on the data analysis, we refer the readers to Supporting Information S2. All the experiments were performed at room temperature.

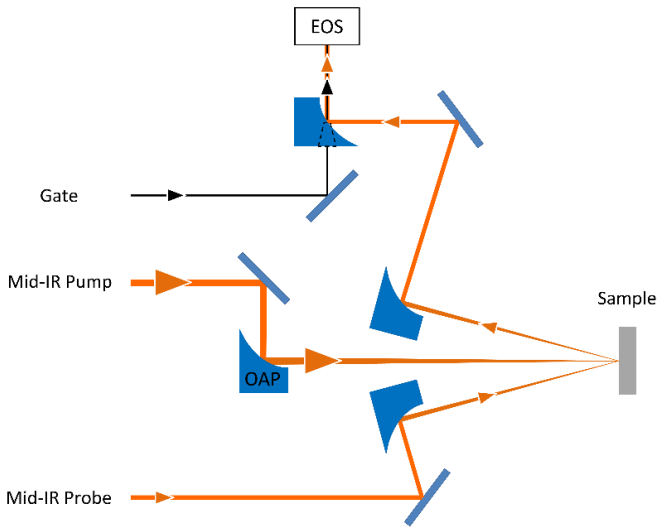

Figure S1-1 Schematic representation of the experiment geometry. Off-axis parabolic mirror (OAP), Electro Optic Sampling (EOS).

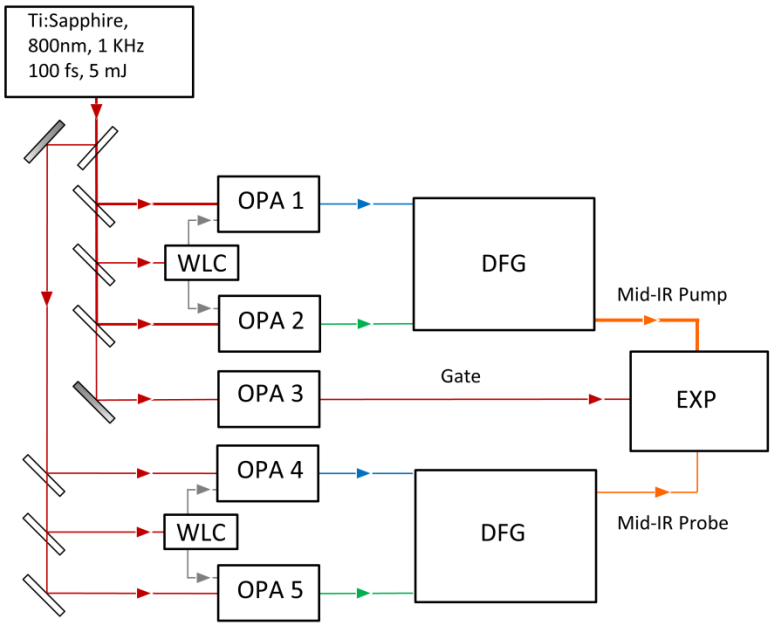

Figure S1-2 | Schematic representation of the set-up used to generate the pump, probe and gate pulses used in the experiment. Optical parametric amplifiers (OPA), white light continuum generation (WLC), difference frequency generation (DFG), experiment (EXP).

S2 – Data Analysis

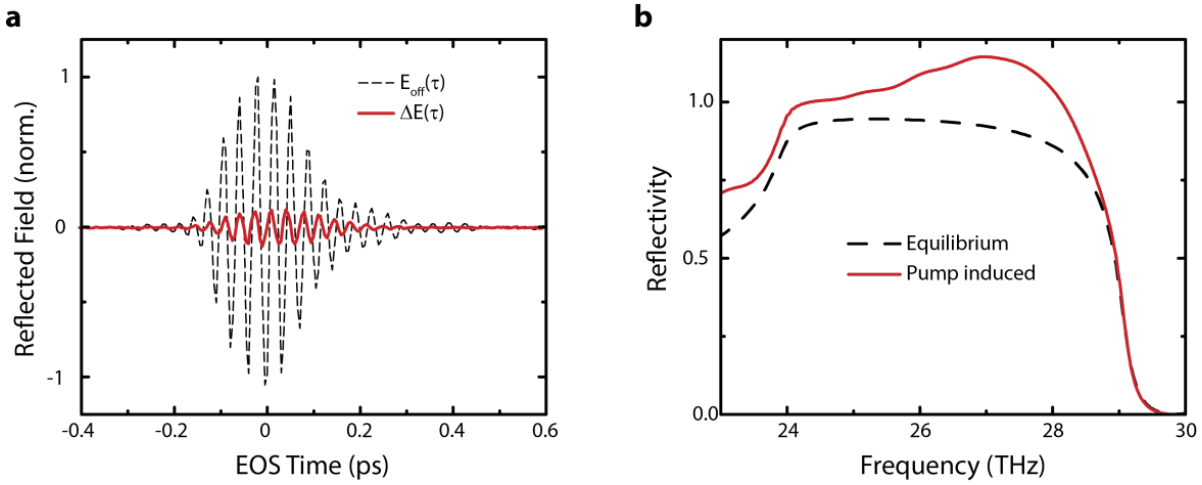

Figure S2-1 (a) Raw data. The dashed line represents the probe electric field $\boldsymbol{E_{off}(\tau)}$ reflected from the sample at equilibrium. The red line represents the simultaneously measured change $\boldsymbol{\Delta E(\tau)}$ induced by the pump pulse. (b) Equilibrium (dashed line) and pump-induced reflectivity (red line) calculated from the data in panel a.

The non-equilibrium reflectivity at any pump-probe delay time *t* can be calculated knowing the probe pulse electric field $E_{off}(\tau)$ reflected from the sample at equilibrium (i.e. without pump) together with the pump-induced change $\Delta E(t,\tau)$, where τ is the EOS time coordinate. The frequency resolved data $E_{off}(\omega)$ and $\Delta E(t,\omega)$ can be reconstructed by Fourier transforming the measured traces along the EOS coordinate τ. The reflectivity is then calculated recalling that $\frac{\Delta E(t,\omega)}{E_{off}(\omega)} = \frac{\Delta r(t,\omega)}{r_{off}(\omega)}$, where $r(t,\omega)$ is the reflection coefficient. Because the equilibrium property $r_{off}(\omega)$ is known, the pump-induced reflection coefficient $r_{on}(\omega) = r_{off}(\omega)(1 + \frac{\Delta r(t,\omega)}{r_{off}(\omega)})$ can be calculated, as well as the reflectivity $R_{on}(\omega)=|r_{on}(\omega)|^2$. Figure S2-1a shows typically measured traces $E_{off}(\omega)$ and $\Delta E(t,\omega)$, leading to the non-equilibrium reflectivity shown in Fig. S2-1b.

In our experiments, these two quantities were measured simultaneously using two lock-in amplifiers, so that the pump-induced change was being constantly referenced to the actual equilibrium reflected field. This automatically renormalized the measurements against thermal

or mechanical drifts of the sample, as well as against slow drifts of the probe pulses carrier-envelope phase (CEP).

The measurements were performed simultaneously chopping at different frequencies the pump and probe beams, with a chopper wheel with 5/7 ratio between the apertures in the inner and outer parts. The probe beam, impinging on the outer part of the wheel, was chopped at 500 Hz (half of the source repetition rate). The pump beam was impinging on the inner part of the wheel. In this configuration, $E_{off}(\tau)$ is measured at 500 Hz, while $\Delta E(\tau)$ is measured at the difference frequency between the inner and outer wheel, which is 143 Hz. Because the response of the lock-in amplifiers at the two frequencies is different, a calibration is required. Indeed, $E_{off}(\tau)$ and $\Delta E(\tau)$ can be measured independently, chopping only the probe beam (without pump impinging on the sample) and only the pump beam, respectively. If these two measurements are done chopping the beams at the same frequency, the measured electric field profiles have the proper relative amplitudes. Thus, these measurements can be used to calibrate those resulting from the double chopping scheme. Figure S2-2a shows $\Delta E(\tau)$ measured chopping only the probe (red) and with the double chopping scheme (black). As expected, because of the different repetition rates, the magnitude of the two signals is different. Fourier transforming the two signals and measuring the amplitude of the FFT peak allows for extracting the calibration factor (2.72 in this case). The comparison between $\Delta E(\tau)$ measured with a single chopper (red) and after renormalizing the double chopping trace (black) is shown in Fig. S2-2b. The measurement of $E_{off}(\tau)$, being carried out at the same chopping frequency of 500 Hz in both cases, does not require a renormalization, as can be seen in Fig. S2-2c, where the signals measured with a single chopper on the probe beam (red) is compared to that measured with double chopping (black).

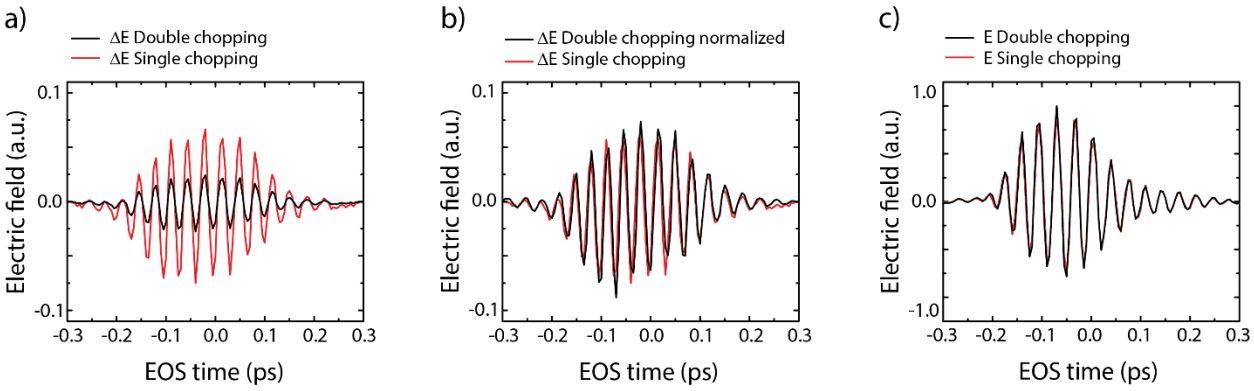

Figure S2-2 (a) $\Delta E(\tau)$ measured chopping only the pump beam (red) and with the double chopping scheme (black). (b) $\Delta E(\tau)$ measured chopping only the pump beam (red) and with the double chopping scheme after calibration (black). (c) $E_{off}(\tau)$ measured chopping only the probe beam (red) and with the double chopping scheme (black).

The measurements shown in Fig.S2-2 were all performed one right after the other, to minimize the detrimental effects on the calibration of mechanical drifts of the sample position or slow drifts of the probe pulses CEP.

This calibration procedure was performed before every measurement, to obtain accurate amplitudes of $E_{off}(\tau)$ and $\Delta E(\tau)$, and therefore calculate a reliable absolute value of the non-equilibrium reflectivity.

S3 – Phase dependence of the signal

According to our model, the Born effective charge and the high frequency dielectric constant depend *quadratically* on the phonon coordinate Q. Their *linear* dependence on Q is not taken into account, as detailed in the Supporting Information S4, because it would correspond to symmetry forbidden terms in the Hamiltonian.

More intuitively, if Z^* and ε_∞ were linearly dependent on Q, when the sample is excited by a laser pulse and the phonon coordinate oscillates around zero, their change would also average to zero, without leading to a net amplification process like the one presented in our work.

Furthermore, if there was *linear component* in the pump-probe signal, the phase of the signal itself would be different if that of the pump was changed by π. Because to leading order the phase of the phonon coordinate Q and that of the pump pulse electric field are the same (bar a constant phase shift due to the pumping close to resonance), changing the pump pulse phase by π corresponds to changing the phonon coordinate oscillations also by π. Hence, the pump-probe signal would change phase when the delay between the pump and probe pulses are delayed by an odd multiple of π.

Because the pump-induced $\Delta E(t, \omega)$ traces have been measured in 50 fs intervals, which corresponds to a 3π phase shift, if the signal was phase-dependent it would change sign every step. Indeed in our case the effect is phase independent, as shown in Fig. S3.

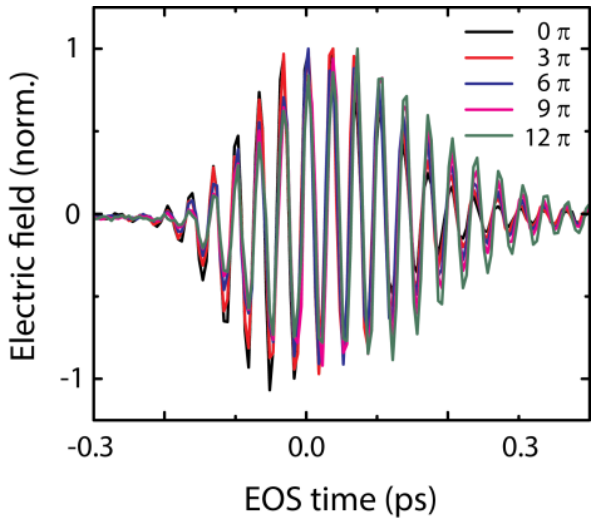

Figure S3 Measured pump-induced changes in the reflected probe electric field profile $\Delta E(\tau)$ for various pump-probe delays. The traces have been all normalized to their maximum value.

This confirms that in our case the phase of the pump-probe signal is independent on that of the pump.

S4 – Model Hamiltonian and DFT calculations

To explore the impact of the phonon excitation on the dielectric properties of 4H-SiC, we used an Hamiltonian which describes the general response of a charged oscillator, representing the infrared active phonon interacting with an electric field. The starting point is the harmonic Hamiltonian, which includes an interaction term between the electric polarization and the electric field as

$$H = \frac{\Omega_{TO}^2}{2} Q^2 - \boldsymbol{P} \cdot \boldsymbol{E} \quad , \tag{S4-1}$$

with P the electric polarization, E the electric field, Q the oscillator coordinate normalized by the unit cell mass and volume, and Ω_{TO}^2 its frequency. There are two contributions to the electric polarization, which are of ionic and electronic origin, respectively. From the modern theory of polarization [6] we can write the sum of both contributions as

$$\boldsymbol{P} = \boldsymbol{Z}^* Q + \epsilon_0 \sum_j (\varepsilon_{ij}^{\infty} - 1)\, \boldsymbol{E}_j \ , \tag{S4-2}$$

Where, ϵ_0 is the vacuum permittivity, $\varepsilon_{ij}^{\infty}$ the permeability tensor for infinite frequencies and $\boldsymbol{Z}^*$ the mode effective charge normalized by the unit cell mass and volume. The latter is related to the Born effective charge tensor by:

$$\boldsymbol{Z}^* = \textstyle\sum_{n,j} \mathbb{Z}_{n,ij}^*\, Q_{n,j} / \sqrt{\sum_{n,j} (Q_{n,j}\, Q_{n,j})} \ . \tag{S4-3}$$

Here the subscript n labels the ions in the unit cell and i, j label the elements of the Born charges tensor, which is of 2nd rank. $Q_{n,j}$ labels the component j of the phonon eigenvector of atom n, which is obtained from the diagonalization of the Harmonic Hamiltonian. Please note that in the harmonic case $\boldsymbol{Z}^*$ itself does not depend on the phonon amplitude but just on the normalized phonon eigenvector. We can combine the expressions above and obtain one expression:

$$H = \frac{\Omega_{TO}^2}{2} Q^2 - \boldsymbol{Z}^* \boldsymbol{E} Q - \frac{1}{2} \epsilon_0 \sum_{j,i} (\varepsilon_{ij}^{\infty} - 1)\, E_j E_i \quad . \tag{S4-4}$$

We next simplify this equation by considering explicitly the physical situation of our experiment and 4H-SiC. Firstly, we note that the Born effective charges and the permeability tensor exhibit

only diagonal components for this material. Secondly, we consider specifically the polarizations of our pump and probe pulses which both exhibit an electric field given as $\boldsymbol{E} = (E, 0,0)$. Furthermore the double degenerate E2 phonon exhibits only components within the plane. Moreover, the two corresponding eigenvectors can be written as Q_1^{E2}=$(Q_n^{E2}, 0,0))$ and Q_2^{E2}=$(0, Q_n^{E2} 0)$. Considering these points, we can simplify equation S4-4 to:

$$H = \frac{\Omega_{TO}^2}{2} Q^2 - Z^* QE - \frac{1}{2}\epsilon_0(\varepsilon_{11}^{\infty} - 1)E^2 \quad . \tag{S4-5}$$

Please note that we are left with only scalar quantities and by the choice of the phonon eigenvector the oscillator charge becomes $\boldsymbol{Z}^* = (Z^*, 0,0)$. Finally, we remark that for convenience we drop the subscript of $\varepsilon_{11}^{\infty}$ and replace it by ε_{∞}.

For small phonon amplitudes the equilibrium optical properties are well described by this Hamiltonian. However, for large driving fields it has to be modified to take into account higher order effects. We therefore expand equation S4-5 up to 4th order considering all the symmetry allowed terms in Q and E. The new Hamiltonian reads:

$$\begin{aligned} H = \left(\frac{\Omega_{TO}^2}{2} + \phi Q^2\right) Q^2 - \left(\frac{\epsilon_0(\varepsilon_{\infty} - 1)}{2} + \beta Q^2 + \xi E^2\right) E^2 \\ - (Z^* + \alpha Q^2 + \theta E^2) QE \quad . \end{aligned} \tag{S4-6}$$

Where ϕ, β, ξ, α and θ are dimensional constants that describe the strength of the nonlinear corrections. Please note that equation S4-6 has been written to highlight in parenthesis the corrections to the terms of equation S4-5.

In the following, we utilize first-principle calculations to reconstruct the change in dielectric properties in 4H-SiC due to the direct phonon excitation. We therefore estimate the relative strength of the expansion coefficients from total energy density functional theory (DFT) calculations, which are mapped on Eqn. (S4-6). All these computations were carried out using DFT within a pseudopotential scheme as implemented in the Quantum Espresso code [7]. We used pseudopotentials generated by the projected augmented wave (PAW) [8] scheme for Si and C which contain as valence states the $3p^2\,3s^2$ and $2p^2\,2s^2$ electrons for each element, respectively. As numerical parameters, we applied a cutoff energy for the plane wave expansion of 75 Rydberg

and 400 Rydberg for the charge density. For all computations, we sampled the Brillouin zone by a 21x21x7 k-point mesh generated with the Monkhorst and Pack scheme [9] and reiterated total energy calculations until the total energy changed less than 10^{-10} Rydberg.

The starting points of the computations are the ground-state dielectric properties of 4H-SiC. Before calculating phonon-modes and Born-effective charges of SiC, we structurally relaxed the unit-cell for forces and pressure below a threshold of 5 μRy/a_0. During the minimization, we constrained the 4H-SiC to the experimentally determined [10] P63mc symmetry. The obtained structure parameters are listed in Tab. S4-1.

Lattice constant		DFT	Expt.
a (Å)		3.06	3.08
c/a		3.272	3.26
Atom	Wyckoff position	DFT	Expt.
Si	2a	0.187	0.187
Si	2b	0.437	0.437
C	2a	0.000	0.000
C	2b	0.250	0.250

Table S4-1: Experimental [10] and calculated (DFT) lattice constants and atomic positions for 4H-SiC. The Wyckoff positions are given according to the P63mc space group.

Starting from this structure, we performed density functional perturbation theory calculations [11] to determine the phonon frequencies, ε_∞ and the Born effective charges. The calculated frequency of the excited E2 phonon mode is 23.3 THz. The eigenvector of this mode displaces Si and C in opposite directions along the hexagonal *a*-axis. The normalized eigenvector of this mode corresponds to a displacement of Si and C about 6 *pm* and 12 *pm*, respectively.

Please regard this value as a reference, which has to be used in combination with the solution of Eqn. (S5-4) to determine the ''real'' displacement of atoms induced by the application of an electric field pulse.

Finally, to determine the coefficients in Eqn. (S4-6) we performed frozen phonon calculations including applied electric fields in the framework of the modern theory of electric polarization. We thereby displaced the structure along the E2 phonon eigenvector and computed the total energy for different applied electric fields. The phonon amplitudes ranged from -1 to 1 times the eigenvector and the electric field from -10 to 10 MV/cm. Finally, we did least mean square minimization of the resulting 2-dimensional energy landscape. Please note that the only parameters allowed to vary within the fit were the additional appearing coefficients in Eqn. (S4-6). Tab. S4-2 summarizes the calculated coefficients, including the equilibrium properties. We further show in Fig. 4-1 the effective changes on the mode effective charge and ϵ_∞ as a function of the phonon mode amplitude Q. Please note that both quantities are associated with the leading order changes in the total energy as given in Tab. S4-2.

To identify the most relevant changes in the energy landscape due to structural modulation we computed the total energy for an electric field of 8 MV/cm and the corresponding phonon amplitude. We then calculated the energy contribution of each term in percent, clearly showing the leading contribution of the α and β terms among the expansion ones.

constant	coefficient	value	Relative energy contribution [%]
Ω_{TO}	Q^2	23 THz	92.6
ε_∞	$-E^2$	5.91	0.2
$Z^*\sqrt{\mu V}$	$-QE$	2.62 e	6.7
α	$-Q^3E$	$3.0\ 10^5\ eV/(u^{\frac{3}{2}}\sqrt{Å}\ MV)$	0.4
β	$-Q^2E^2$	$1.75\ 10^{11}\ eV/(u\ MV^2)$	0.1
θ	$-QE^3$	$6.24\ 10^{14}\ \sqrt{Å}\ eV/(MV^3\sqrt{u})$	<< 0.1
ξ	$-E^4$	$3.26\ 10^{13}\ cm\ eV/MV^4$	<< 0.1
ϕ	$-Q^4$	$1.2\ 10^{-3}\ eV/(u^2\ Å)$	<< 0.1

Table S4-2: List of the coefficients contained in Eqn. (S4-6) as computed from DFT total energies. Furthermore, we show the relative energy contribution from each term for an applied electric field of 8 MV/cm and corresponding Q phonon amplitude.

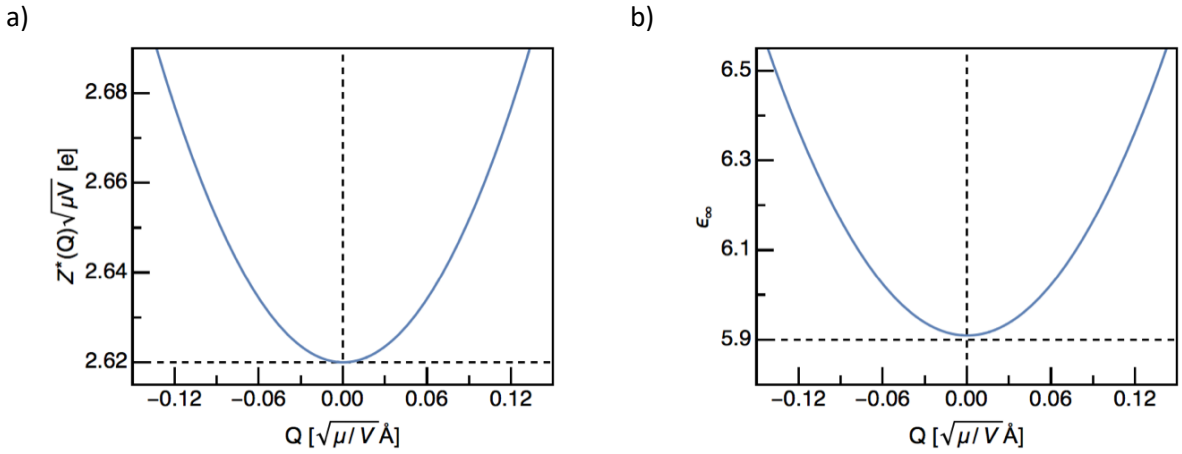

Fig. S4-1: Modulation of the mode effective charge (a) and ϵ_∞ (b) as a function of the phonon mode amplitude Q for 4H-SiC. The range on the horizontal axis is comparable to the phonon amplitudes reached in our experiments.

S5 – Simulation of the nonlinear optical properties

The time-dependent and frequency-dependent reflectivity, as well as the *E* and Q amplification shown in Fig. 5 and Fig. 6 of the main text were calculated solving Maxwell's equations in space and time with the one-dimensional finite difference time domain method (1D-FDTD) [12]. The discretization of time and space was done according to the Yee Grid [13], which is suitable for the solution of Maxwell's equation in the absence of free charges, since it intrinsically satisfies the divergence equations $\vec{\nabla} \cdot \vec{B} = 0$ and $\vec{\nabla} \cdot \vec{E} = 0$. The curl equations were explicitly implemented in the FDTD loop, and perfectly absorbing boundary conditions at the end of the grid were used. Being the sample non-magnetic, the constitutive equation for the magnetic field was $\vec{B} = \mu_0 \vec{H}$.

Because these simulations are used to reproduce the sample optical properties, it is important to note that the Born Effective charge can be expressed in terms of optically measurable quantities such as the phonon eigenfrequency Ω_{TO}, the static dielectric function ε_0 and the high frequency permittivity ε_∞ via the relation $Z^* = \Omega_{TO}\sqrt{\epsilon_0(\varepsilon_0 - \varepsilon_\infty)}$, where ϵ_0 denotes the vacuum permittivity.

The equilibrium optical properties of SiC were therefore introduced in our simulations through the constitutive equation $D = \epsilon_0 E + P$, with the polarization in the sample calculated as $P = \epsilon_0(\varepsilon_\infty - 1)E + \Omega_{TO}\sqrt{\epsilon_0(\varepsilon_0 - \varepsilon_\infty)}Q$.

The values for Ω_{TO} (23.92 THz), the damping coefficient Γ (0.2 THz), and ε_0 (9.66) were extracted from a Lorentz fit to the static reflectivity data [5], using as a fixed parameter the value of ε_∞ found in the literature [14]. Similarly, the dynamics of the phonon coordinate was introduced in the FDTD loop with the equation of motion $\ddot{Q} + \Gamma\dot{Q} + \Omega_{TO}^2 Q = \Omega_{TO}\sqrt{\epsilon_0(\varepsilon_0 - \varepsilon_\infty)}E$.

The non-equilibrium optical properties were calculated using the Hamiltonian shown in Supporting Information S4. Considering only the α and β expansion terms, which are shown to be the leading ones in Supporting Information S4, the Hamiltonian can be written (as a function of optically measurable quantities) in the form

$$H = \frac{1}{2}\Omega_{TO}^2 Q^2 - \frac{1}{2}\epsilon_0(\varepsilon_\infty - 1)E^2 - \Omega_{TO}\sqrt{\epsilon_0(\varepsilon_0 - \varepsilon_\infty)}QE - \alpha Q^3 E - \beta Q^2 E^2, \quad \text{S5-1}$$

and the nonlinear polarization can be expressed as

$$P = -\frac{\partial H}{\partial E} = \epsilon_0(\varepsilon_\infty - 1)E + \Omega_{TO}\sqrt{\epsilon_0(\varepsilon_0 - \varepsilon_\infty)}Q + \alpha Q^3 + 2\beta Q^2 E, \quad \text{S5-2}$$

which is the equation implemented in the FDTD loop. The force acting on the oscillator Q derived from the same Hamiltonian is

$$F_q = -\frac{\partial H}{\partial Q} = -\Omega_{TO}^2 Q^2 + \Omega_{TO}\sqrt{\epsilon_0(\varepsilon_0 - \varepsilon_\infty)}E + 3\alpha Q^2 E + 2\beta Q E^2, \quad \text{S5-3}$$

and therefore the equation of motion for the phonon coordinate becomes

$$\ddot{Q} + \Gamma\dot{Q} + \Omega_{TO}^2 Q = \Omega_{TO}\sqrt{\epsilon_0(\varepsilon_0 - \varepsilon_\infty)}E + 3\alpha Q^2 E + 2\beta Q E^2, \quad \text{S5-4}$$

which was discretized and implemented in our FDTD simulations.

To simulate the non-linear pump-probe response of the sample, sets of three simulations were performed for each pump-probe delay. The first simulation was considering both the pump (strong) and the probe (weak) field impinging on the sample, and the reflected field E_{PP} was being recorded. A second and a third simulation were then performed, considering only the pump and only the probe field, respectively, therefore calculating the reflected fields E_{Pump} and E_{probe}.

The field reflected from the sample in the pumped state was then calculated as $E_{On} = E_{PP} - E_{Pump}$, after making sure that the probe field was weak enough not to drive the system in a nonlinear regime. This was done checking that the reflectivity calculated from E_{probe} was identical to that calculated without nonlinearities.

The reflected field from the unperturbed sample was then calculated as $E_{Off} = E_{probe}$.

From these fields it was possible to obtain $\frac{\Delta_r}{r} = \frac{E_{on} - E_{off}}{E_{off}}$ and calculate the reflectivity in the same way as detailed in Supporting Information S2 for the experimental data.

The direct comparison of the EOS traces measured experimentally and simulated with the procedure presented here is reported in Fig. S5, showing good agreement.

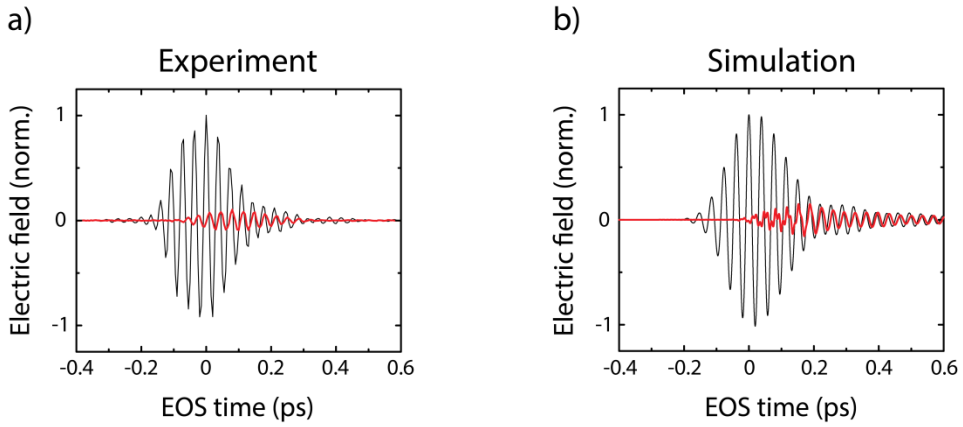

Figure S5 Direct comparison of the experimental (panel a) and simulated (panel b) probe electric field reflected from the sample at equilibrium (black lines) and pump induced changes at the maximum of the pump-probe response (red lines) for a pump peak electric field of 5.9 MV/cm.

S6 – Independent modulation of Z^* and ε_∞

The modulations of Z^* and ε_∞ cannot be disentangled experimentally, because they involve similar contributions to the energy of the system and therefore happen simultaneously. However, the separate effects of the two nonlinearities can be explored by activating them independently in the simulations.

The modulation of the Born effective charge is expected to add a 3ω component to the driving term in the ions equation of motion and can be expected to induce amplification, as discussed in the main text of the paper. The results of simulations in which only $Z^*$is modulated (α ≠ 0, β = 0) are reported in Fig. S6-1 and support this hypothesis.

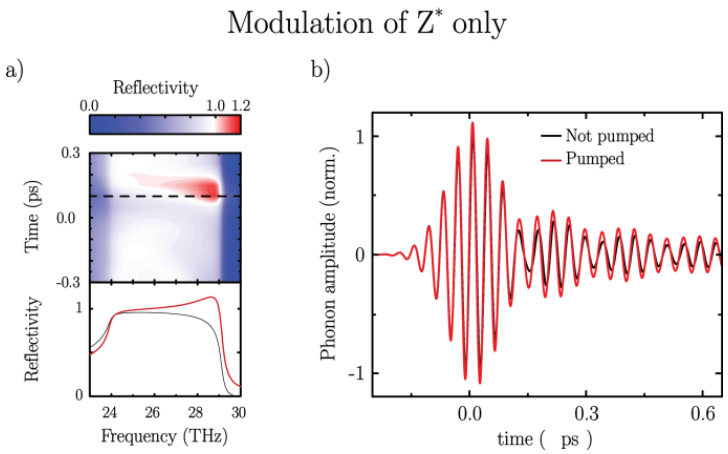

Figure S6-1 Effects on the non-equilibrium reflectivity (a) and phonon coordinate oscillations (b) due to the modulation of the Born effective charge alone.

Figure S6-1a shows the time dependent and frequency dependent reflectivity R for an applied peak electric field of 8.7 MV/cm, where the value of α was chosen to reach a maximum reflectivity of 1.15, to mimic the experimental results. The color plot in the upper panel of Fig.S6-1a shows areas in which the reflectivity is increased above one, highlighted in red by the color scale. However, the frequency cut at the maximum of the pump-probe response depicted in the lower panel shows a different behavior with respect to the experiments. Here, the reflectivity is mostly increased at Ω_{LO} = 29 THz rather than in the center of the reststrahlen band. Nonetheless, the reflectivity increasing above one is concomitant with an amplification of the phonon coordinate oscillations, as reported in Fig. S6-1b. This simulation supports the hypothesis that

the Z^* modulation can lead to an amplification of the optical phonon, but does not reproduce well the measured reflectivity features.

The modulation of $\boldsymbol{\varepsilon}_\infty$ alone, on the other hand, is expected to turn the ions equation of motion into that of a parametric oscillator, which is also supporting the parametric amplification of the phonon coordinate oscillations. This hypothesis is supported by the results of simulations in which only $\boldsymbol{\varepsilon}_\infty$ is modulated ($\alpha = 0$, $\beta \neq 0$), reported in Fig.S6-2.

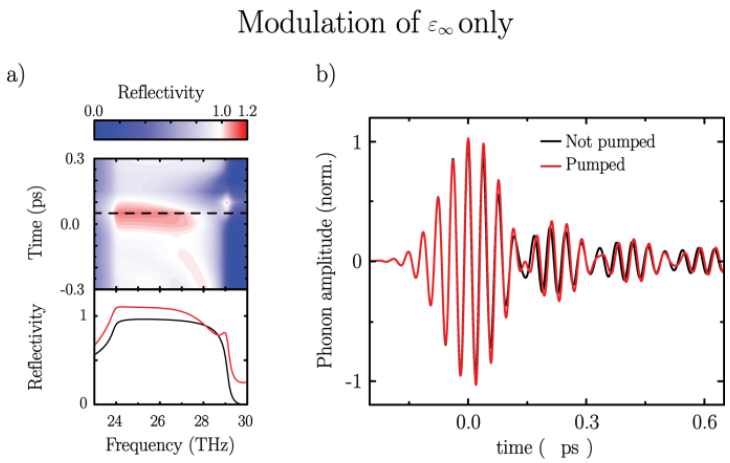

Figure S6-2 Effects on the non-equilibrium reflectivity (a) and phonon coordinate oscillations (b) due to the modulation of ε_∞ alone

Also here the value of β was chosen to reach a maximum reflectivity of 1.15 for an applied peak electric field of 8.7 MV/cm. The color plot showing the time and frequency dependent reflectivity in the upper panel of Fig. S6-2a also shows areas in which the reflectivity is increased above one. In this case, however, the frequency cut at the maximum of the pump-probe response depicted in the lower panel shows a different behavior, with the reflectivity mostly enhanced around Ω_{TO}= 24 THz. The phonon coordinate oscillations, reported in Fig. S6-2b, are amplified also in this case. The simulations reported here show that the modulations of $Z^*$and $\boldsymbol{\varepsilon}_\infty$ taken singularly, albeit causing the increase of reflectivity above one and the amplification of the ionic motions, cannot properly reproduce the experimental results. This is consistent with our model, in which both these modulations need to be taken into account, as they entail same order of magnitude contributions to the energy density.

S7 – Frequency dependent pumping efficiency

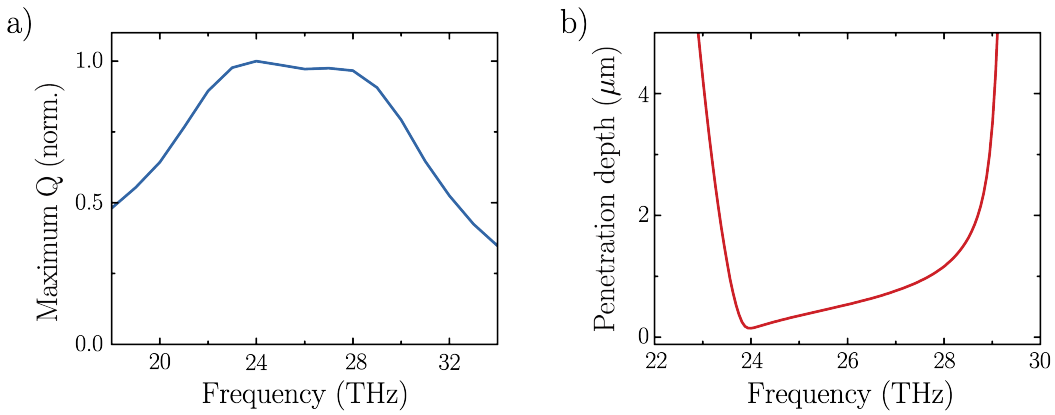

Figure S7-1 (a) Maximum value reached by the phonon coordinate Q as a function of the pumping frequency. (b) Frequency dependent light penetration depth.

Figure S7-1a shows the pump frequency dependent maximum phonon amplitude Q in SiC, considering the bandwidth of the pump pulses used in our experiments. The plot shows that Q has an almost flat response in correspondence with the reststrahlen band. Two relative maxima are evident within such broad peak, one at 24 THz, corresponding to Ω_{TO}, and one at 29 THz, corresponding to Ω_{LO} . The first maximum is due to the *mechanical* response of the phonon oscillator, which at Ω_{TO}, is driven exactly at resonance. Hence, for a constant force on the atoms, the largest motion is found at this frequency. The second maximum, on the other hand, is due to an increase of the electric field E in the sample given by the zero crossing of ε_r happening at Ω_{LO}. In this case, even if the mechanical oscillator is driven farther from resonance, the very large driving force is responsible for the high amplitude reached by Q, which is 90 % of that at Ω_{TO}. The large bandwidth of the pump pulses is then responsible for the merging of these two effects in the broad profile of Fig. S7-1a. To determine the frequency at which the effect of the pump pulses on the probe is maximized, the value of Q discussed so far has to be combined with the light penetration depth inside the sample, shown in Fig. S7-1b. At Ω_{LO} the large amplitude driving of Q is combined with a penetration depth of around 4 μm, thus leading to a higher amplification of the probe pulses, and thus to a better signal to noise.

For this reason, the pump pulses in our experiments were tuned at 29 THz, as shown in figure S7-2.

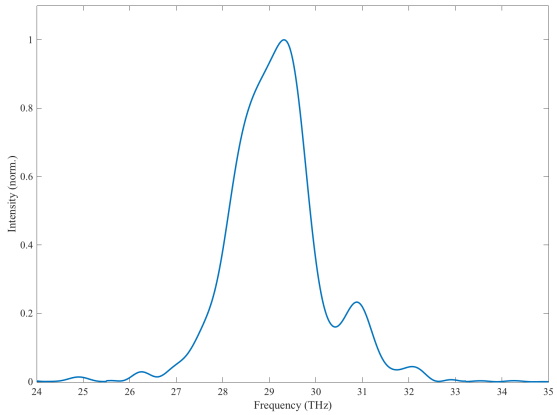

Figure S7-2 Spectrum of the pump pulses used in the experiments.

References

[1] G. Cerullo, A. Baltuška, O. D. Mücke, and C. Vozzi, Laser Photonics Rev. **5**, 323 (2011).

[2] A. Sell, A. Leitenstorfer, and R. Huber, Opt. Lett. **33**, 2767 (2008).

[3] C. Manzoni, D. Polli, and G. Cerullo, Rev. Sci. Instrum. **77**, 23103 (2006).

[4] K. Iwaszczuk, D. G. Cooke, M. Fujiwara, H. Hashimoto, and P. Uhd Jepsen, Opt. Express **17**, 21969 (2009).

[5] W. G. Spitzer, D. Kleinman, and D. Walsh, Phys. Rev. **113**, 127 (1959).

[6] X. Gonze and C. Lee, Phys. Rev. B **55**, 10355 (1997).

[7] P. Giannozzi, S. Baroni, N. Bonini, M. Calandra, R. Car, C. Cavazzoni, D. Ceresoli, G. L. Chiarotti, M. Cococcioni, I. Dabo, A. Dal Corso, S. de Gironcoli, S. Fabris, G. Fratesi, R. Gebauer, U. Gerstmann, C. Gougoussis, A. Kokalj, M. Lazzeri, L. Martin-Samos, N. Marzari, F. Mauri, R. Mazzarello, S. Paolini, A. Pasquarello, L. Paulatto, C. Sbraccia, S. Scandolo, G. Sclauzero, A. P. Seitsonen, A. Smogunov, P. Umari, and R. M. Wentzcovitch, J. Phys. Condens. Matter **21**, 395502 (2009).

[8] P. E. Blöchl, Phys. Rev. B **50**, 17953 (1994).

[9] J. D. Pack and H. J. Monkhorst, Phys. Rev. B **16**, 1748 (1977).

[10] J. M. Bind, Mater. Res. Bull. **13**, 91 (1978).

[11] S. Baroni, S. de Gironcoli, A. Dal Corso, and P. Giannozzi, Rev. Mod. Phys. **73**, 515 (2001).

[12] A. Taflove and S. C. Hagness, Artech House 1038 (2005).

[13] K. Yee, Antennas Propagation, IEEE Trans. **14**, 302 (1966).

[14] L. Patrick and W. J. Choyke, Phys. Rev. B **2**, 2255 (1970).